

# High-field Breakdown and Thermal Characterization of Indium Tin Oxide Transistors

Haotian Su<sup>1,†</sup>, Yuan-Mau Lee<sup>2,†</sup>, Tara Peña<sup>1</sup>, Sydney Fultz-Waters<sup>2</sup>, Jimin Kang<sup>1</sup>, Çağıl Köroğlu<sup>1</sup>, Sumaiya Wahid<sup>1</sup>, Christina J. Newcomb<sup>3</sup>, Young Suh Song<sup>1</sup>, H.-S. Philip Wong<sup>1</sup>, Shan X. Wang<sup>1,2</sup>, and Eric Pop<sup>1,2,4,5,\*</sup>

<sup>1</sup>*Department of Electrical Engineering, Stanford University, Stanford, CA 94305, USA*

<sup>2</sup>*Department of Materials Science and Engineering, Stanford University, Stanford, CA 94305, USA*

<sup>3</sup>*Stanford Nano Shared Facilities, Stanford University, Stanford, CA 94305, USA*

<sup>4</sup>*Department of Applied Physics, Stanford University, Stanford, CA 94305, USA*

<sup>5</sup>*Precourt Institute for Energy, Stanford University, CA 94305, USA*

<sup>†</sup>*Authors contributed equally.* \*Contact: [epop@stanford.edu](mailto:epop@stanford.edu)

**ABSTRACT:** Amorphous oxide semiconductors are gaining interest for logic and memory transistors compatible with low-temperature fabrication. However, their low thermal conductivity and heterogeneous interfaces suggest that their performance may be severely limited by self-heating, especially at higher power and device densities. Here, we investigate the high-field breakdown of amorphous indium tin oxide (ITO) transistors with scanning thermal microscopy (SThM) and multiphysics simulations. The ITO devices break irreversibly at channel temperatures of  $\sim 180$  °C and  $\sim 340$  °C on SiO<sub>2</sub> and HfO<sub>2</sub> substrates, respectively, but failure appears primarily caused by thermally-induced compressive strain near the device contacts. Combining SThM measurements with simulations allows us to estimate a thermal boundary conductance (TBC) of  $35 \pm 12$  MWm<sup>-2</sup>K<sup>-1</sup> for ITO on SiO<sub>2</sub>, and  $51 \pm 14$  MWm<sup>-2</sup>K<sup>-1</sup> for ITO on HfO<sub>2</sub>. The latter also enables significantly higher breakdown power due to better heat dissipation and closer thermal expansion matching. These findings provide valuable insights into the thermo-mechanical limitations of ITO devices, paving the way for more reliable and high-performance amorphous oxide transistors.

**KEYWORDS:** High-field Breakdown, ITO Transistor, SThM, Strain

---

## INTRODUCTION

Amorphous oxide semiconductors (AOS) are well-established in the display industry<sup>1-3</sup> and are increasingly recognized as promising back-end-of-line (BEOL)-compatible channel materials for thin-film transistors.<sup>4-6</sup> Among them, indium tin oxide (ITO) transistors stand out due to their low-temperature large-scale deposition methods, high drive current, and low leakage, making them promising for BEOL logic and memory applications.<sup>4,7-11</sup> However, their performance and stability could be limited by self-heating effects during operation,<sup>11-16</sup> with heat dissipation challenges potentially worsened by high power and high device densities.<sup>17-23</sup>

To address the heat dissipation challenges in oxide transistors, various strategies have been explored. P. Y. Liao *et al.*<sup>14</sup> incorporated an interlayer between channel and substrate to facilitate device heat dissipation, while K. Kise *et al.*<sup>24</sup> used a U-shaped transistor design to mitigate self-heating. Furthermore, high thermal conductivity substrates, such as high-resistivity Si, SiC, and diamond, have been employed to aid heat dissipation and alleviate self-heating effects.<sup>11,13,15,25</sup>

Despite these advancements, the heat dissipation and breakdown mechanisms in ITO transistors remain poorly understood. Moreover, the thermal boundary conductance (TBC) at the interface between the ITO channel and its dielectric, essential for transistor heat dissipation,<sup>26-29</sup> is underexplored. Techniques like thermoreflectance imaging and time-domain thermoreflectance have been widely used to study the thermal properties of devices and thin films.<sup>13,25,30-32</sup> However, their limitations, such as low spatial resolution (i.e. spot size greater than transistor dimensions) and considerable uncertainties in TBC measurements for interfaces between ultrathin amorphous films, highlight the need for alternative approaches to understand the thermal properties and breakdown mechanisms of ITO transistors.

In this study, we fabricate ITO transistors with 4 nm thin sputtered channels and investigate their breakdown during high-field operation. Using scanning thermal microscopy (SThM),<sup>33,34</sup> we measure the ITO channel temperature during operation and, through simulations, quantify the TBC at ITO/SiO<sub>2</sub> and ITO/HfO<sub>2</sub> interfaces. These interfaces limit heat dissipation and, along with their thermal expansion mismatch, contribute to localized compressive strain. Our analysis reveals that the breakdown of ITO transistors is driven by thermally-accelerated cracks that appear near the ITO channel/contact edges. These findings provide insights into the thermo-mechanical limitations of ITO transistors and inform the design of more reliable future devices.

## METHODS

We employ an electro-thermo-mechanical multiphysics approach to investigate the failure mechanisms and heat dissipation in ITO transistors, as depicted in **Figure 1**. Electrical analysis begins with the fabrication of back-gated ITO transistors, using a 4 nm thick sputtered ITO channel on a SiO<sub>2</sub> (100 nm) on p<sup>++</sup> Si substrate with Ni top contacts. The highly-doped Si substrate is also used as the back-gate and more fabrication details can be found in S. Wahid *et al.*<sup>10</sup> and Supporting Information **Section S1**. Nearly one hundred devices were characterized electrically, up to their breakdown, with channel lengths ( $L$ ) between 1.5 to 1.7  $\mu\text{m}$  and widths of 10  $\mu\text{m}$ .

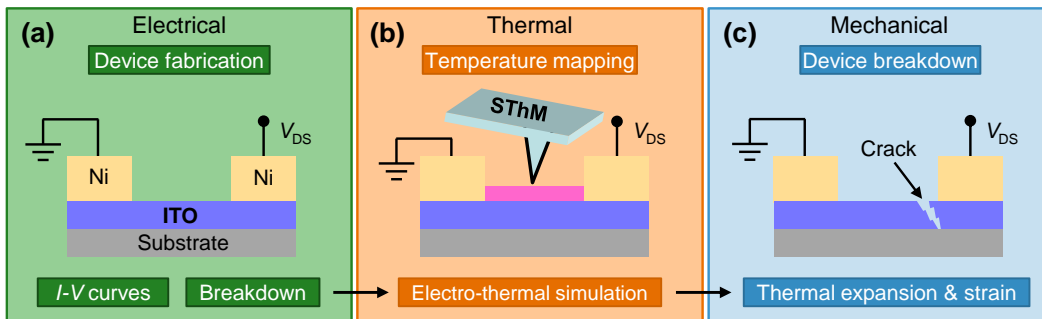


**Figure 1.** Overview of our electro-thermo-mechanical multiphysics approach. Electrical analysis begins with (a) ITO transistor fabrication, measuring current-voltage up to device breakdown. Thermal analysis in (b) is done with scanning thermal microscopy (SThM), combined with finite-element electro-thermal modeling, to extract thermal properties such as the thermal boundary conductance (TBC) of the ITO/SiO<sub>2</sub> interface. Solid mechanics simulations, (c), reveal thermal expansion and peak strain distributions which appear consistent with images of cracks forming in the ITO channel, leading to device failure.

To map the device temperature during operation we used SThM,<sup>27,35-37</sup> which has sub-100 nm spatial resolution, depending on the probing tip and environmental conditions used. These thermal measurements were complemented with finite-element modeling,<sup>27,28,38</sup> which enabled the

simulation of device temperatures and the estimation of some unknown parameters, such as TBC. Additionally, simulations of mechanical strain distributions across the transistor<sup>39,40</sup> were conducted to assess the impact of thermal expansion during operation. Comparing these simulations with experimental observations of device failure correlates electrical performance, heat dissipation, and mechanical reliability in our ITO transistors.

## RESULTS AND DISCUSSION

### Electrical Characterization

ITO transistors with the geometry illustrated in **Figure 2a** were fabricated and characterized to evaluate their electrical performance and breakdown behavior. Transfer curves ( $I_D$  vs.  $V_{GS}$ ) shown in **Figure 2b** were measured over 30 devices with a channel length of  $\sim 1.6 \mu\text{m}$ , revealing relatively low variability. Breakdown measurements were conducted on a subset of 10 devices by applying  $V_{GS} = 45 \text{ V}$  and sweeping  $V_{DS}$  from 0 V to 40 V. Transfer curves measured after breakdown, in **Figure 2c**, show much lower on-state current and a loss of gate control. Scanning electron microscopy (SEM) images further revealed the physical damage in these transistors: **Figure 2d** compares an original device channel with failed devices in **Figure 2e** (prominent cracks in the ITO channel near the drain) and **Figure 2f** (additional cracks in the Ni drain contact).

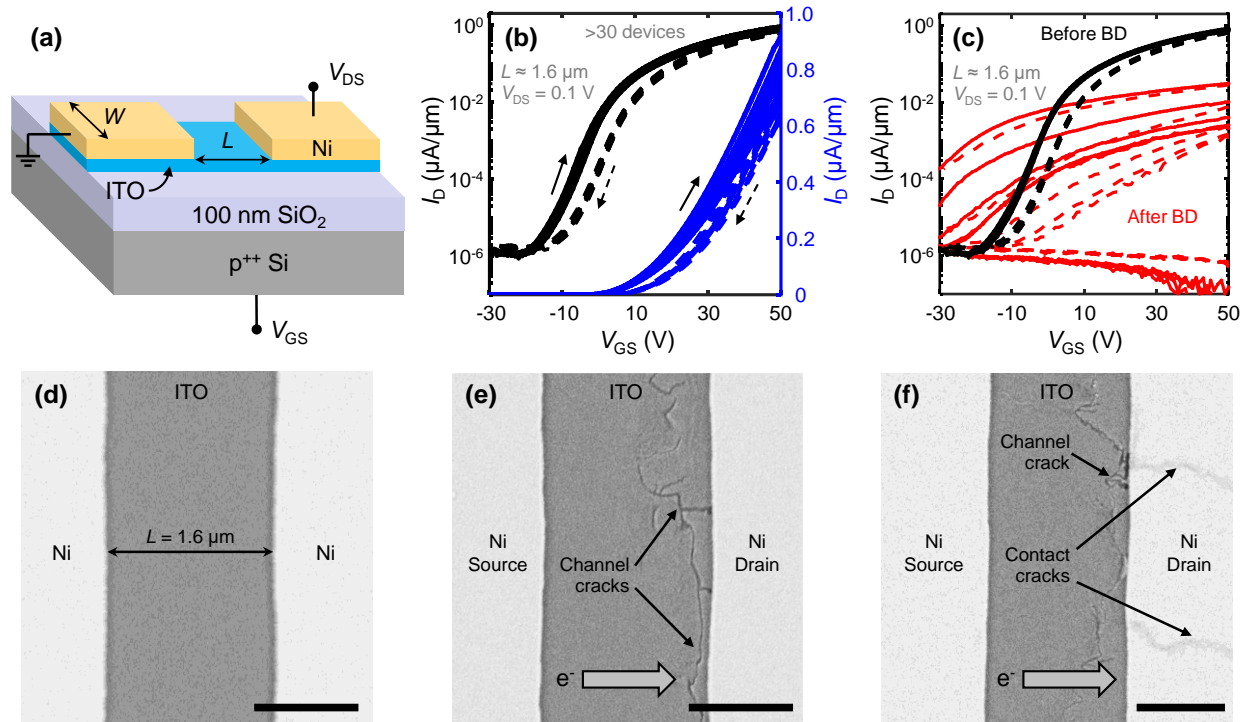


**Figure 2.** (a) Schematic of back-gated ITO transistors used in this study, with 4 nm thin ITO channel sputtered on SiO<sub>2</sub> (100 nm)/Si (p<sup>++</sup>) substrate, and 80 nm Ni source and drain contacts. (b) Measured transfer curves from over 30 devices with channel length  $L \approx 1.6 \mu\text{m}$ , on logarithmic (black) and linear scale (blue). (c) Transfer curves for a subset of 10 devices before (black) and after breakdown (red), showing a significant reduction in on-state  $I_D$  and loss of gate control. Solid/dashed lines mark forward/backward  $V_{GS}$  sweeps. (d) Scanning electron microscopy (SEM) image of initial ITO transistor channel compared with (e) SEM image of a device after breakdown showing channel cracks, and (f) another device showing additional cracks under the Ni drain. Scale bars in (d-f) are all 1  $\mu\text{m}$ . Block arrows in (e, f) show the direction of electron flow.

Current vs. drain voltage ( $V_{DS}$ ) measurements up to device breakdown are shown in **Figures 3a–b**, with different gate voltages ( $V_{GS}$ ); in **Figure 3a**, devices are operated below threshold ( $V_{GS} = -15, 0$  V) and at smaller overdrive ( $V_{GS} = 15$  V). Below threshold,  $I_D$  increases weakly with  $V_{DS}$  due to carrier extraction from trap states under increasing lateral electric field, consistent with previous reports for AOS-based power devices.<sup>41–43</sup> However, for device breakdowns in the on-state (**Figure 3b** with  $V_{GS} = 45, 60, 75$  V), an abrupt current drop is observed at  $V_{DS} \approx 20$  V, similar to breakdown behavior recently reported in  $\sim 10$  times larger and thicker IGZO devices.<sup>44</sup> Additional details on transfer curves and gate leakage before and after breakdown are provided in Supporting Information **Section S2**. The average electric field at breakdown ( $\mathcal{E}_{BD}$ ) along the ITO channel decreases with increasing  $V_{GS}$  (**Figure 3c**), suggesting that the breakdown is initiated by higher current and higher temperature (i.e. higher carrier density at higher  $V_{GS}$ ) rather than the lateral electric field acting alone. The corresponding breakdown power ( $P_{BD}$ ) in **Figure 3d** displays a weak increase with  $V_{GS}$ , which is consistent with improved field uniformity as the transistor breaks down deeper in the linear regime at higher  $V_{GS}$ . Nevertheless, as we will later see, the ITO channel breakdown mechanism is more complex.

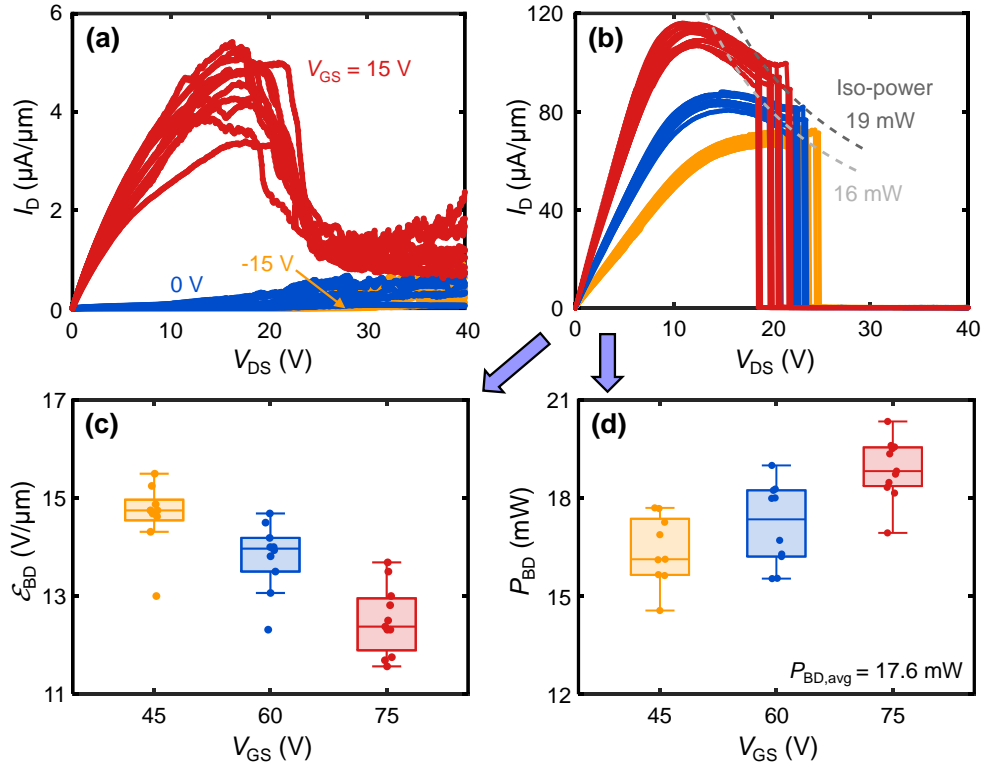


**Figure 3.** (a) Measured current vs. drain voltage ( $I_D$ – $V_{DS}$ ) curves of ITO transistors in sub-threshold or low overdrive ( $V_{GS} = -15, 0, 15$  V). (b)  $I_D$ – $V_{DS}$  breakdown of ITO transistors at high  $V_{GS} = 45, 60, 75$  V, showing an abrupt  $I_D$  drop around  $V_{DS} \approx 20$  V;  $\sim 10$  devices were measured for each  $V_{GS}$ . Dashed lines mark the range of power dissipation at device breakdown. (c) Average lateral electric field at device breakdown ( $\mathcal{E}_{BD}$ ) along the ITO channel, from the three  $V_{GS}$  conditions in (b). (d) Breakdown power ( $P_{BD}$ ) under the same breakdown  $V_{GS}$  in (b), with average breakdown power  $P_{BD,avg} \approx 17.6$  mW.

### Thermal Characterization

To evaluate the device temperature during operation, we employ scanning thermal microscopy (SThM). The experimental setup, shown schematically in **Figure 4a**, utilizes a Wheatstone bridge

to connect the SThM cantilever, which operates in contact mode. Devices were capped with a 6 nm  $\text{Al}_2\text{O}_3$  layer to prevent direct electrical contact<sup>27,35,36</sup> between the SThM probe and ITO channel. More details on the SThM setup and calibration are provided in Supporting Information **Section S3**. The transfer curves of uncapped and  $\text{Al}_2\text{O}_3$ -capped devices (**Figure 4b**) reveal a negative shift in threshold voltage for the capped devices, consistent with our prior findings.<sup>10</sup> This capping layer has negligible impact on the ITO channel temperature measured by SThM.<sup>27</sup> For SThM measurements, to prevent device damage or breakdown, the devices were measured in the linear  $I_D$  vs.  $V_{DS}$  region, a subset of which is shown in **Figure 4c**.

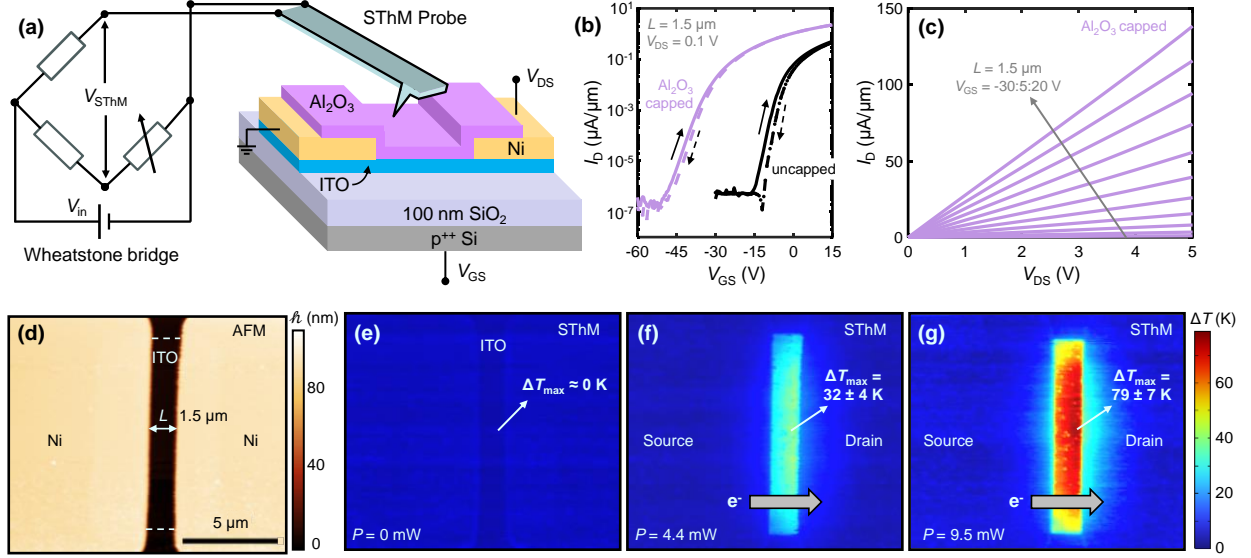


**Figure 4.** (a) Schematic of SThM measurement on ITO transistors, showing a Wheatstone bridge connected to the SThM cantilever. The tip scans in contact mode with the top device surface. (b) Measured transfer curves of uncapped (black) and  $\text{Al}_2\text{O}_3$ -capped (purple) devices, showing negative shift in threshold voltage consistent with our previous work.<sup>10</sup> Solid/dashed lines mark forward/backward  $V_{GS}$  sweeps. (c) Measured  $I_D$  vs.  $V_{DS}$  curve of  $\text{Al}_2\text{O}_3$ -capped devices, showing linear behavior. (d) AFM topography scan of an ITO transistor, and corresponding SThM temperature map at input powers of: (e) 0 mW, (f) 4.4 mW, and (g) 9.5 mW. The block arrow shows the direction of electron flow, from source to drain. At an input power of 9.5 mW, the maximum ITO temperature rise ( $\Delta T_{\max}$ , above room temperature) is  $79 \pm 7$  K, as shown in (g).

The atomic force microscopy (AFM) topography scan of an ITO transistor with 1.5  $\mu\text{m}$  long channel is shown in **Figure 4d**. The corresponding SThM temperature maps (**Figures 4e–g**) display temperature distributions at different input powers,  $P = I_D V_{DS}$ . **Figure 4e**, at 0 mW, displays the background temperature rise  $\sim 0$  K, as expected. At 4.4 mW and 9.5 mW input powers,  $\Delta T_{\max}$  reaches  $32 \pm 4$  K and  $79 \pm 7$  K, respectively. The uncertainties arise from SThM calibration, with more details in Supporting Information **Section S3**. The measured temperature is slightly higher near the drain contact, which is expected due to the direction of electron flow.<sup>27</sup> (The electron density is lower and the lateral field is higher near the drain.) The temperature drops rapidly at the Ni contacts, which function as efficient heat sinks.

### Finite-Element Electro-Thermo-Mechanical Modeling

We also carried out finite-element simulations<sup>27,28,38</sup> to complement the SThM measurements and understand the heat dissipation characteristics of ITO transistors. The simulated temperature map



with 9.5 mW input power is shown in **Figure 5a**, revealing a peak temperature rise  $\Delta T_{\max} = 71.7$  K. This simulation uses thermal conductivity ( $k$ ) and thermal boundary conductance (TBC) values detailed in Supporting Information **Section S4**. We also performed a sensitivity analysis with respect to some of the key thermal simulation parameters – as shown in **Figure 5b**,  $\Delta T_{\max}$  has negligible dependence on practical  $k$  ranges for  $\text{Al}_2\text{O}_3$ , Ni, and ITO. Similarly, **Figure 5c** indicates that wide TBC variations (25–250  $\text{MWm}^{-2}\text{K}^{-1}$ ) for ITO-Ni, ITO- $\text{Al}_2\text{O}_3$ , and Ni- $\text{Al}_2\text{O}_3$  interfaces have minimal impact on  $\Delta T_{\max}$ , suggesting those interfaces play a minimal role in heat sinking. However,  $\Delta T_{\max}$  is strongly dependent on the TBC of the ITO- $\text{SiO}_2$  interface, which is estimated to be  $35 \pm 12 \text{ MWm}^{-2}\text{K}^{-1}$ , by comparing our simulations with SThM measurements of the peak temperature ( $79 \pm 7$  K in **Figure 4g**) for this power input. The  $\text{TBC}_{\text{ITO-SiO}_2}$  is estimated here for the first time, and is consistent with other TBCs reported for similar interfaces.<sup>14,45</sup>

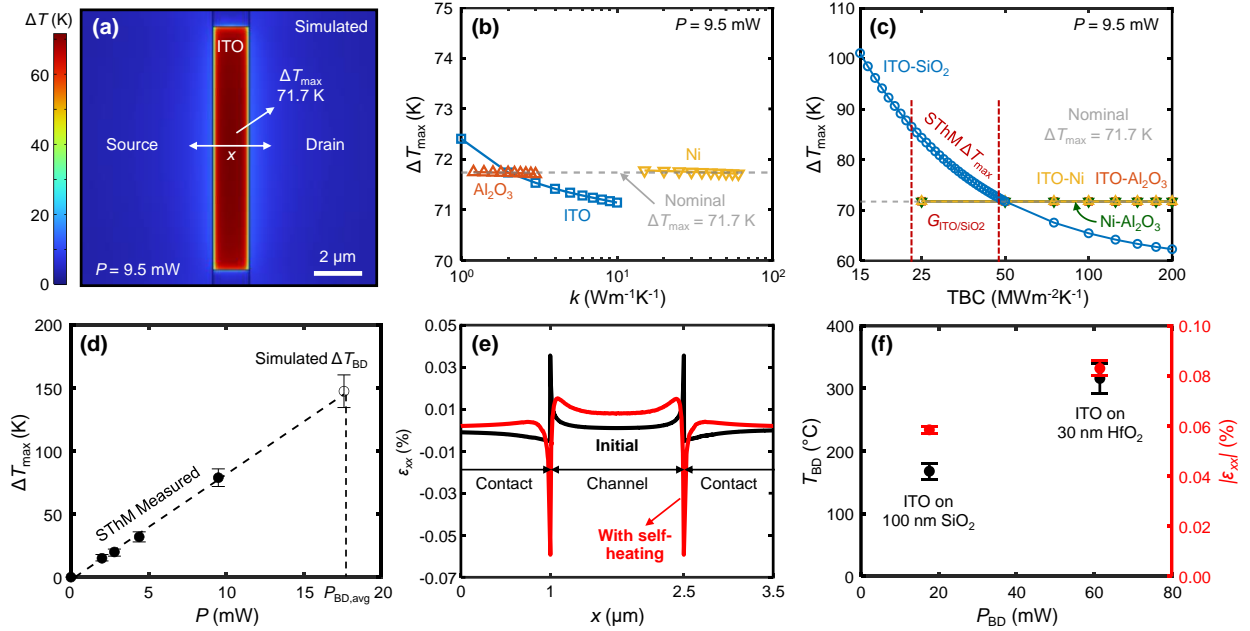


**Figure 5.** (a) Simulated temperature map of ITO transistor with 9.5 mW input power, showing peak temperature rise  $\Delta T_{\max} = 71.7$  K, with nominal thermal parameters provided in Supporting Information **Section S4**. (b) Sensitivity analysis of  $\Delta T_{\max}$  for the same device, with respect to the expected thermal conductivity ( $k$ ) range of  $\text{Al}_2\text{O}_3$ , Ni, and ITO. (c) Sensitivity analysis of  $\Delta T_{\max}$  with respect to TBC at material interfaces, showing minimal dependence on TBC at ITO-Ni, ITO- $\text{Al}_2\text{O}_3$ , and Ni- $\text{Al}_2\text{O}_3$  interfaces. However,  $\Delta T_{\max}$  varies with the TBC of ITO- $\text{SiO}_2$  interface, estimated to be  $35 \pm 12 \text{ MWm}^{-2}\text{K}^{-1}$  by comparing to the SThM measurements. (d) Dependence of  $\Delta T_{\max}$  on input power,  $P$ . Filled symbols mark SThM-measured temperature, hollow symbol is a simulation of  $\Delta T_{\max}$  at  $P_{\text{BD,avg}}$  from in **Figure 3d**. Dashed line is a linear fit, to highlight the trend. (e) Initial strain distribution ( $\epsilon_{xx}$ ) along the ‘ $x$ ’ white arrow in panel (a), showing tensile strain in the ITO channel and compressive strain under contacts (black curve). At device breakdown with self-heating, the compressive strain peaks at the channel/contact edge (red curve). (f) Summary of breakdown temperature ( $T_{\text{BD}}$ ) and peak compressive strain ( $|\epsilon_{xx}|$ ) vs. breakdown power for ITO transistors on 100 nm  $\text{SiO}_2$  and on 30 nm  $\text{HfO}_2$  dielectric, on Si back-gate.

**Figure 5d** shows the relationship between  $\Delta T_{\max}$  and input power ( $P$ ), demonstrating good agreement between temperatures measured by SThM and simulated temperature at the average breakdown power ( $P_{\text{BD,avg}}$ , determined in **Figure 3d**). The average breakdown temperature ( $T_{\text{BD}}$ ) of our ITO transistors on 100 nm  $\text{SiO}_2/\text{Si}$  substrate is found to be  $\sim 155\text{--}181$  °C. This temperature is lower

than the annealing temperature of ITO transistors,<sup>9,10</sup> which can reach up to 300 °C. Therefore, we cannot attribute the breakdown of our ITO transistors solely to the temperature rise during operation, and other mechanisms must be at play. To understand other effects, we also carried out thermo-mechanical simulations, displaying the estimated strain distribution along the ITO channel,  $\epsilon_{xx}$ , before current flow (black line) and after  $P_{BD,avg}$  is applied (red line), as shown in **Figure 5e**. Initially, tensile strain is observed near the channel-contact edges and compressive strain appears under the contacts, which is attributed to the presence of Ni contacts.<sup>40</sup> (We report stress from a 80 nm evaporated Ni layer in Supporting Information **Section S5**.) With  $P_{BD,avg}$  input power the device self-heats and the mismatch in coefficient of thermal expansion (CTE,  $\alpha$ ) between ITO ( $\alpha_{ITO} \approx 8 \times 10^{-6} \text{ K}^{-1}$ )<sup>46,47</sup> and  $\text{SiO}_2$  ( $\alpha_{\text{SiO}_2} \approx 5.6 \times 10^{-7} \text{ K}^{-1}$ )<sup>48,49</sup> generates compressive strain at the channel edges (red lines in **Figure 5e**). The position of these compressive strain peaks correspond to the locations of channel cracks seen in the SEM images from **Figures 2e-f**.

### Discussion and Comparison to ITO on $\text{HfO}_2$

We note that the  $\sim 0.06\%$  compressive strain suggested by our device simulations is lower than typical crack onset strain (COS) values previously reported for ITO, which range from 0.1% to several percent.<sup>50-54</sup> Part of this may be due to non-uniformities in our devices and contacts (e.g. Ni contact grains or non-uniform current flow at high input power), which cannot be captured by simulations that assume uniform material properties. In addition, the COS is also expected to depend on ITO thickness, substrate, and deposition conditions, and most reported COS values were under externally applied mechanical stresses. In contrast, cracking of ultrathin ITO due to compressive strain induced by electrical self-heating has not been previously explored.

Our findings suggest that the cracking failure of these ultrathin ITO transistors on  $\text{SiO}_2$  is caused by the CTE mismatch between ITO and  $\text{SiO}_2$ , and initiated by self-heating effects during device operation. This CTE mismatch generates compressive strain near the channel edges, which appears to exceed the reduced COS of the ITO material at the elevated temperature. We also note that the low crystallization temperature of ITO ( $\sim 150\text{-}200 \text{ }^\circ\text{C}$ )<sup>50,51,55-58</sup> may accelerate structural changes during device self-heating, such as grain boundary formation and localized (e.g. filamentary) crystallization.<sup>11</sup> A previous study<sup>51</sup> also suggested that defects and grain boundaries, often introduced during low-temperature annealing, can act as stress concentrators, accelerating crack formation. These microstructural changes, coupled with thermal and electrical stresses, likely create a cascading effect that weakens the ITO channel and promotes crack formation.

For comparison, we also fabricated ITO transistors on 30 nm  $\text{HfO}_2$  on Si ( $p^{++}$ ) substrates, with more details provided in Supporting Information **Section S6**. Electrical and SThM characterizations, along with finite-element simulations, were performed following the same methodology as described in **Figure 4** and **Figure 5**. The thermal boundary conductance (TBC) at the ITO/ $\text{HfO}_2$  interface was  $51 \pm 14 \text{ MWm}^{-2}\text{K}^{-1}$ , a value obtained in this study for the first time. While this  $\text{TBC}_{\text{ITO}/\text{HfO}_2}$  value is nearly 50% higher than the  $\text{TBC}_{\text{ITO}/\text{SiO}_2}$ , it still falls on the lower end of typical TBC values for material interfaces.<sup>59-62</sup> SThM measurements and simulations (Supporting Information **Section S6**) further revealed that the breakdown temperature of ITO transistors on 30 nm  $\text{HfO}_2$  lies between 292 °C and 340 °C, nearly double the  $T_{BD}$  of ITO transistors on 100 nm  $\text{SiO}_2$  substrate (both on Si). Despite the higher  $T_{BD}$ , the maximum compressive strain at device breakdown was estimated to be only  $\sim 0.086\%$ , attributed to the closer CTE matching between ITO ( $\alpha_{\text{ITO}} \approx 8 \times 10^{-6} \text{ K}^{-1}$ ) and  $\text{HfO}_2$  ( $\alpha_{\text{HfO}_2} \approx 6 \times 10^{-6} \text{ K}^{-1}$ ).<sup>63,64</sup> **Figure 5f** highlights these differences by

summarizing the  $T_{BD}$  and peak compressive strain ( $|\varepsilon_{xx}|$ ) at the breakdown power for ITO transistors on both substrates. These findings suggest that ITO transistors on 30 nm HfO<sub>2</sub> have better heat dissipation and reduced thermal stress, enabling them to sustain higher power before breakdown. These results highlight the importance of efficient heat dissipation and CTE matching<sup>65</sup> in optimizing material systems for high-performance ITO transistors.

## CONCLUSION

We investigated the high-field breakdown of ITO transistors using an electro-thermo-mechanical multiphysics approach. Comparing scanning thermal microscopy measurements with simulations, we obtained the steady-state device temperature and estimated the thermal boundary conductance (TBC) at the ITO/SiO<sub>2</sub> interface,  $35 \pm 12 \text{ MWm}^{-2}\text{K}^{-1}$ . This relatively low TBC, combined with the significant mismatch in coefficient of thermal expansion (CTE) between ITO and SiO<sub>2</sub>, induces localized compressive strain near the contacts and leads to device breakdown. It is also possible that the low crystallization temperature of ITO amplifies microstructural changes, such as grain boundary formation, and further accelerates mechanical failure under thermal and electrical stress. For comparison, we also fabricated ITO transistors on 30 nm HfO<sub>2</sub>, on the same Si back-gate substrates. The ITO/HfO<sub>2</sub> thermal boundary conductance is found to be  $51 \pm 14 \text{ MWm}^{-2}\text{K}^{-1}$ , approximately 50% higher than for ITO/SiO<sub>2</sub>, which, combined with the thinner dielectric and closer CTE matching to ITO, enabled higher device breakdown power and temperature. Overall, this study provides critical insights into the interplay of electrical, thermal, and mechanical factors in ITO transistors, underscoring the importance of heat dissipation and thermal stress management for high-performance, robust thin-film transistors.

## SUPPORTING INFORMATION

Supporting information includes fabrication process flow (Section S1), additional electrical breakdown characteristics (Section S2), scanning thermal microscopy details (Section S3), finite-element electro-thermo-mechanical modeling (Section S4), wafer-scale Ni stress characterization (Section S5), and devices on 30 nm HfO<sub>2</sub> dielectric (Section S6).

## AUTHOR DECLARATIONS

### Author Contributions

H.S. and Y.L. designed the experiments, supported by E.P. H.S. and Y.L. fabricated the samples and performed electrical characterization with support from T.P., J.K., and S.W. H.S. performed SThM measurements and conducted finite-element simulations with input from S.F.-W., Ç.K., and E.P. H.S. wrote the initial manuscript, with input from Y.L. and E.P. All authors discussed the results and edited the manuscript.

### Conflict of Interest

The authors have no conflicts to disclose.

### Acknowledgments

Several authors were supported by PRISM and SUPREME, JUMP 2.0 centers sponsored by the Semiconductor Research Corporation (SRC) and DARPA. This work was also supported in part by the National Science Foundation under Grant No. 2345655 in the Partnerships for Innovation



(PFI) program. The authors also acknowledge partial support from the Stanford Nonvolatile Memory Technology Research Initiative (NMTRI) Affiliates program. Part of this work was performed at Stanford Nanofabrication Facility (SNF) and Stanford Nano Shared Facilities (SNSF), supported by the National Science Foundation under award ECCS-2026822.

## DATA AVAILABILITY

The data that support the findings of this study are available from the corresponding author upon reasonable request.

## REFERENCES

- (1) Nomura, K.; Ohta, H.; Takagi, A.; Kamiya, T.; Hirano, M.; Hosono, H. Room-temperature fabrication of transparent flexible thin-film transistors using amorphous oxide semiconductors. *Nature* **2004**, *432* (7016), 488-492. DOI: 10.1038/nature03090.
- (2) Kamiya, T.; Hosono, H. Material characteristics and applications of transparent amorphous oxide semiconductors. *Npg Asia Mater* **2010**, *2* (1), 15-22. DOI: 10.1038/asiamat.2010.5.
- (3) Park, J. S.; Maeng, W.-J.; Kim, H.-S.; Park, J.-S. Review of recent developments in amorphous oxide semiconductor thin-film transistor devices. *Thin Solid Films* **2012**, *520* (6), 1679-1693. DOI: 10.1016/j.tsf.2011.07.018.
- (4) Liu, S.; Jana, K.; Toprasertpong, K.; Chen, J.; Liang, Z.; Jiang, Q.; Wahid, S.; Qin, S.; Chen, W.-C.; Wong, H. S. P. Gain Cell Memory on Logic Platform – Device Guidelines for Oxide Semiconductor Transistor Materials Development. In 2023 International Electron Devices Meeting (IEDM), 2023. DOI: 10.1109/iedm45741.2023.10413726.
- (5) Hikake, K.; Li, Z.; Hao, J.; Pandey, C.; Saraya, T.; Hiramoto, T.; Takahashi, T.; Uenuma, M.; Uraoka, Y.; Kobayashi, M. A Nanosheet Oxide Semiconductor FET Using ALD InGaO<sub>x</sub> Channel and InSnO<sub>x</sub> Electrode with Normally-off Operation, High Mobility and Reliability for 3D Integrated Devices. In 2023 IEEE Symposium on VLSI Technology and Circuits (VLSI Technology and Circuits), 2023. DOI: 10.23919/VLSITechnologyandCir57934.2023.10185234.
- (6) Hosono, H.; Kumomi, H. *Amorphous Oxide Semiconductors*; 2022. DOI: 10.1002/9781119715641.
- (7) Li, S.; Tian, M.; Gao, Q.; Wang, M.; Li, T.; Hu, Q.; Li, X.; Wu, Y. Nanometre-thin indium tin oxide for advanced high-performance electronics. *Nat Mater* **2019**, *18* (10), 1091-1097. DOI: 10.1038/s41563-019-0455-8.
- (8) Toprasertpong, K.; Liu, S.; Chen, J.; Wahid, S.; Jana, K.; Chen, W.-C.; Li, S.; Pop, E.; Philip Wong, H. S. Co-designed Capacitive Coupling-Immune Sensing Scheme for Indium-Tin-Oxide (ITO) 2T Gain Cell Operating at Positive Voltage Below 2 V. In 2023 IEEE Symposium on VLSI Technology and Circuits (VLSI Technology and Circuits), 2023. DOI: 10.23919/VLSITechnologyandCir57934.2023.10185433.
- (9) Wahid, S.; Daus, A.; Kumar, A.; Philip Wong, H. S.; Pop, E. First Demonstration of Dual-Gated Indium Tin Oxide Transistors with Record Drive Current  $\sim 2.3$  mA/ $\mu$  m at  $L \approx 60$  nm and  $V_{DS} = 1$  V. In 2022 International Electron Devices Meeting (IEDM), 2022. DOI: 10.1109/iedm45625.2022.10019544.
- (10) Wahid, S.; Daus, A.; Kwon, J.; Qin, S.; Ko, J.-S.; Wong, H. S. P.; Pop, E. Effect of Top-Gate Dielectric Deposition on the Performance of Indium Tin Oxide Transistors. *IEEE Electron Device Letters* **2023**, *44* (6), 951-954. DOI: 10.1109/led.2023.3265316.

- (11) Hu, Q.; Gu, C.; Liu, S.; Zeng, M.; Zhu, S.; Kang, J.; Liu, R.; Zhao, W.; Tong, A.; Li, Q.; et al. First Demonstration of Top-Gate Indium-Tin-Oxide RF Transistors with Record High Cut-off Frequency of 48 GHz,  $I_d$  of 2.32 mA/ $\mu\text{m}$  and gm of 900  $\mu\text{S}/\mu\text{m}$  on SiC Substrate with Superior Reliability at 85 °C. In 2023 International Electron Devices Meeting (IEDM), 2023. DOI: 10.1109/iedm45741.2023.10413673.
- (12) Urakawa, S.; Tomai, S.; Ueoka, Y.; Yamazaki, H.; Kasami, M.; Yano, K.; Wang, D.; Furuta, M.; Horita, M.; Ishikawa, Y.; et al. Thermal analysis of amorphous oxide thin-film transistor degraded by combination of joule heating and hot carrier effect. *Appl Phys Lett* **2013**, *102* (5). DOI: 10.1063/1.4790619.
- (13) Liao, P.-Y.; Alajlouni, S.; Si, M.; Zhang, Z.; Lin, Z.; Noh, J.; Wilk, C.; Shakouri, A.; Ye, P. D. Thermal Studies of BEOL-compatible Top-Gated Atomically Thin ALD  $\text{In}_2\text{O}_3$  FETs. In 2022 IEEE Symposium on VLSI Technology and Circuits (VLSI Technology and Circuits), 2022. DOI: 10.1109/VLSITechnologyandCir46769.2022.9830279.
- (14) Liao, P.-Y.; Khot, K.; Alajlouni, S.; Snure, M.; Noh, J.; Si, M.; Zhang, Z.; Shakouri, A.; Ruan, X.; Ye, P. D. Alleviation of Self-Heating Effect in Top-Gated Ultrathin  $\text{In}_2\text{O}_3$  FETs Using a Thermal Adhesion Layer. *Ieee T Electron Dev* **2023**, *70* (1), 113-120. DOI: 10.1109/ted.2022.3221358.
- (15) Liao, P.-Y.; Zheng, D.; Alajlouni, S.; Zhang, Z.; Si, M.; Zhang, J.; Lin, J.-Y.; Feygelson, T. I.; Tadjer, M. J.; Shakouri, A.; et al. Transient Thermal and Electrical Co-Optimization of BEOL Top-Gated ALD  $\text{In}_2\text{O}_3$  FETs Toward Monolithic 3-D Integration. *Ieee T Electron Dev* **2023**, *70* (4), 2052-2058. DOI: 10.1109/ted.2023.3235313.
- (16) Charnas, A.; Zhang, Z.; Lin, Z.; Zheng, D.; Zhang, J.; Si, M.; Ye, P. D. Review-Extremely Thin Amorphous Indium Oxide Transistors. *Adv Mater* **2024**, *36* (9), e2304044. DOI: 10.1002/adma.202304044.
- (17) Sabry Aly, M. M.; Gao, M.; Hills, G.; Lee, C.-S.; Pitner, G.; Shulaker, M. M.; Wu, T. F.; Asheghi, M.; Bokor, J.; Franchetti, F.; et al. Energy-Efficient Abundant-Data Computing: The N3XT 1,000x. *Computer* **2015**, *48* (12), 24-33. DOI: 10.1109/mc.2015.376.
- (18) Srimani, T.; Bechdolt, A.; Choi, S.; Gilardi, C.; Kasperovich, A.; Li, S.; Lin, Q.; Malakoutian, M.; McEwen, P.; Radway, R. M.; et al. N3XT 3D Technology Foundations and Their Lab-to-Fab: Omni 3D Logic, Logic+Memory Ultra-Dense 3D, 3D Thermal Scaffolding. In 2023 International Electron Devices Meeting (IEDM), 2023. DOI: 10.1109/iedm45741.2023.10413794.
- (19) K orođlu,  .; Pop, E. High Thermal Conductivity Insulators for Thermal Management in 3D Integrated Circuits. *IEEE Electron Device Letters* **2023**, *44* (3), 496-499. DOI: 10.1109/led.2023.3240676.
- (20) Wong, H. S. P.; Akarvardar, K.; Antoniadis, D.; Bokor, J.; Hu, C.; King-Liu, T.-J.; Mitra, S.; Plummer, J. D.; Salahuddin, S. A Density Metric for Semiconductor Technology [Point of View]. *Proceedings of the IEEE* **2020**, *108* (4), 478-482. DOI: 10.1109/jproc.2020.2981715.
- (21) Zhang, Y.; Sarvey, T. E.; Bakir, M. S. Thermal challenges for heterogeneous 3D ICs and opportunities for air gap thermal isolation. In 2014 International 3D Systems Integration Conference (3DIC), 2014. DOI: 10.1109/3dic.2014.7152174.
- (22) Diaz, C. H. Logic Technology Device Innovations. In 2024 International Electron Devices Meeting (IEDM), 2024.
- (23) Gabourie, A. J.; Polanco, C. A.; McClellan, C. J.; Su, H.; Malakoutian, M.; Koroglu, C.; Chowdhury, S.; Donadio, D.; Pop, E. AI-Accelerated Atoms-to-Circuits Thermal Simulation Pipeline for Integrated Circuit Design. In 2024 International Electron Devices Meeting (IEDM), 2024.

- (24) Kise, K.; Fujii, M. N.; Bermundo, J. P.; Ishikawa, Y.; Uraoka, Y. Self-Heating Suppressed Structure of a-IGZO Thin-Film Transistor. *IEEE Electron Device Letters* **2018**, *39* (9), 1322-1325. DOI: 10.1109/led.2018.2855152.
- (25) Lin, J. Y.; Zhang, Z.; Alajlouni, S.; Liao, P. Y.; Lin, Z.; Niu, C.; Shakouri, A.; Ye, P. D. First Determination of Thermal Resistance and Thermal Capacitance of Atomic-Layer-Deposited In<sub>2</sub>O<sub>3</sub> Transistors. In 2023 International Electron Devices Meeting (IEDM), 2023. DOI: 10.1109/iedm45741.2023.10413835.
- (26) Gabourie, A. J.; Köroğlu, Ç.; Pop, E. Substrate-dependence of monolayer MoS<sub>2</sub> thermal conductivity and thermal boundary conductance. *J Appl Phys* **2022**, *131* (19). DOI: 10.1063/5.0089247.
- (27) Yalon, E.; McClellan, C. J.; Smithe, K. K. H.; Munoz Rojo, M.; Xu, R. L.; Suryavanshi, S. V.; Gabourie, A. J.; Neumann, C. M.; Xiong, F.; Farimani, A. B.; et al. Energy Dissipation in Monolayer MoS<sub>2</sub> Electronics. *Nano Lett* **2017**, *17* (6), 3429-3433. DOI: 10.1021/acs.nanolett.7b00252.
- (28) Daus, A.; Vaziri, S.; Chen, V.; Köroğlu, Ç.; Grady, R. W.; Bailey, C. S.; Lee, H. R.; Schauble, K.; Brenner, K.; Pop, E. High-performance flexible nanoscale transistors based on transition metal dichalcogenides. *Nat Electron* **2021**, *4* (7), 495-501. DOI: 10.1038/s41928-021-00598-6.
- (29) Huang, J.; Li, Y.; Yu, X.; Liu, Z.; Wang, F.; Yue, Y.; Zhang, R.; Dai, R.; Yang, K.; Liu, H.; et al. Improved Thermal Dissipation in a MoS<sub>2</sub> Field-Effect Transistor by Hybrid High-k Dielectric Layers. *ACS Appl Mater Interfaces* **2024**, *16* (45), 62527-62536. DOI: 10.1021/acsami.4c12143.
- (30) Jiang, P.; Qian, X.; Yang, R. Tutorial: Time-domain thermoreflectance (TDTR) for thermal property characterization of bulk and thin film materials. *J Appl Phys* **2018**, *124* (16). DOI: 10.1063/1.5046944.
- (31) Kwon, H.; Perez, C.; Park, W.; Asheghi, M.; Goodson, K. E. Thermal Characterization of Metal-Oxide Interfaces Using Time-Domain Thermoreflectance with Nanograting Transducers. *ACS Appl Mater Interfaces* **2021**, *13* (48), 58059-58065. DOI: 10.1021/acsami.1c12422.
- (32) Su, H.; Kwon, H.; Xue, F.; Sato, N.; Bhat, U.; Tsai, W.; Bosman, M.; Asheghi, M.; Goodson, K. E.; Pop, E.; et al. Thermal Characterization of Ultrathin MgO Tunnel Barriers. *Nano Lett* **2024**. DOI: 10.1021/acs.nanolett.4c02571.
- (33) Zhang, Y.; Zhu, W.; Hui, F.; Lanza, M.; Borca - Tasciuc, T.; Muñoz Rojo, M. A Review on Principles and Applications of Scanning Thermal Microscopy (S<sub>Th</sub>M). *Advanced Functional Materials* **2019**, *30* (18). DOI: 10.1002/adfm.201900892.
- (34) Swoboda, T.; Wainstein, N.; Deshmukh, S.; Koroglu, C.; Gao, X.; Lanza, M.; Hilgenkamp, H.; Pop, E.; Yalon, E.; Munoz Rojo, M. Nanoscale temperature sensing of electronic devices with calibrated scanning thermal microscopy. *Nanoscale* **2023**, *15* (15), 7139-7146. DOI: 10.1039/d3nr00343d.
- (35) Datye, I. M.; Rojo, M. M.; Yalon, E.; Deshmukh, S.; Mleczko, M. J.; Pop, E. Localized Heating and Switching in MoTe<sub>2</sub>-Based Resistive Memory Devices. *Nano Lett* **2020**, *20* (2), 1461-1467. DOI: 10.1021/acs.nanolett.9b05272.
- (36) Deshmukh, S.; Rojo, M. M.; Yalon, E.; Vaziri, S.; Koroglu, C.; Islam, R.; Iglesias, R. A.; Saraswat, K.; Pop, E. Direct measurement of nanoscale filamentary hot spots in resistive memory devices. *Sci Adv* **2022**, *8* (13), eabk1514. DOI: 10.1126/sciadv.abk1514.
- (37) Yalon, E.; Deshmukh, S.; Munoz Rojo, M.; Lian, F.; Neumann, C. M.; Xiong, F.; Pop, E. Spatially Resolved Thermometry of Resistive Memory Devices. *Sci Rep* **2017**, *7* (1), 15360. DOI: 10.1038/s41598-017-14498-3.

- (38) Su, H.; Kwon, H.; Hwang, W.; Xue, F.; K ro glu,  .; Tsai, W.; Asheghi, M.; Goodson, K. E.; Wang, S. X.; Pop, E. Thermal optimization of two-terminal SOT-MRAM. *J Appl Phys* **2024**, *136* (1). DOI: 10.1063/5.0211620.
- (39) Jaikissoon, M.; K ro glu,  .; Yang, J. A.; Neilson, K.; Saraswat, K. C.; Pop, E. CMOS-compatible strain engineering for monolayer semiconductor transistors. *Nat Electron* **2024**, *7* (10), 885-891. DOI: 10.1038/s41928-024-01244-7.
- (40) Hoang, L.; Jaikissoon, M.; Koroglu, C.; Zhang, Z.; Bennett, R. K. A.; Song, J. H.; Yang, J. A.; Ko, J. S.; Brongersma, M. L.; Saraswat, K. C.; et al. Understanding the Impact of Contact-Induced Strain on the Electrical Performance of Monolayer WS<sub>2</sub> Transistors. *Nano Lett* **2024**, *24* (41), 12768-12774. DOI: 10.1021/acs.nanolett.4c02616.
- (41) Deng, S.; Kwak, J.; Lee, J.; Aabrar, K. A.; Kim, T.-H.; Choe, G.; Kirtania, S. G.; Zhang, C.; Li, W.; Phadke, O.; et al. BEOL Compatible Oxide Power Transistors for On-Chip Voltage Conversion in Heterogenous 3D (H3D) Integrated Circuits. In 2023 International Electron Devices Meeting (IEDM), 2023. DOI: 10.1109/iedm45741.2023.10413838.
- (42) Wu, W.; Huang, T.; Yang, G.; Cao, J.; Yu, Z.; Sun, H.; Xu, Y.; Sun, W. High-Voltage Indium-Tin-Oxide Thin-Film Transistors Possessing Drift Region Capped With Indium-Tin-Oxide Layer. *IEEE Electron Device Letters* **2024**, *45* (7), 1201-1204. DOI: 10.1109/led.2024.3394888.
- (43) Xie, J.; Wang, Y.; Zheng, Z.; Kang, Y.; Chen, X.; Zheng, G.; Shao, R.; Han, K.; Gong, X. Top-Gate Indium-Tin-Oxide Power Transistors Featuring High Breakdown Voltage of 156 V. *IEEE Electron Device Letters* **2024**, *45* (10), 1847-1850. DOI: 10.1109/led.2024.3435428.
- (44) Yang, H.; Huang, T.; Pan, W.; Lu, L.; Zhang, S. Output breakdown characteristics of amorphous InGaZnO thin-film transistors at high gate voltage. *Appl Phys Lett* **2024**, *124* (9). DOI: 10.1063/5.0188427.
- (45) Feng, T.; Zhou, H.; Cheng, Z.; Larkin, L. S.; Neupane, M. R. A Critical Review of Thermal Boundary Conductance across Wide and Ultrawide Bandgap Semiconductor Interfaces. *ACS Appl Mater Interfaces* **2023**, *15* (25), 29655-29673. DOI: 10.1021/acsami.3c02507.
- (46) Choi, S. K.; Lee, J. I. Effect of film density on electrical properties of indium tin oxide films deposited by dc magnetron reactive sputtering. *Journal of Vacuum Science & Technology A: Vacuum, Surfaces, and Films* **2001**, *19* (5), 2043-2047. DOI: 10.1116/1.1371326.
- (47) Krataithong, C.; Srichai, K.; Wongrat, E.; Tubtimtae, A. Comparative study on the influence of transparent glass substrates for antimony telluride thin films via structural and optical properties. *Journal of Science: Advanced Materials and Devices* **2022**, *7* (3). DOI: 10.1016/j.jsamd.2022.100449.
- (48) El-Kareh, B. *Fundamentals of Semiconductor Processing Technology*; 1995. DOI: 10.1007/978-1-4615-2209-6.
- (49) Luo, S.; Cullen, C. P.; Guo, G.; Zhong, J.; Duesberg, G. S. Investigation of growth-induced strain in monolayer MoS<sub>2</sub> grown by chemical vapor deposition. *Applied Surface Science* **2020**, *508*. DOI: 10.1016/j.apsusc.2019.145126.
- (50) Leterrier, Y.; M dico, L.; Demarco, F.; M nson, J. A. E.; Betz, U.; Escol , M. F.; Kharrazi Olsson, M.; Atamny, F. Mechanical integrity of transparent conductive oxide films for flexible polymer-based displays. *Thin Solid Films* **2004**, *460* (1-2), 156-166. DOI: 10.1016/j.tsf.2004.01.052.
- (51) Oh, S. J.; Kwon, J. H.; Lee, S.; Choi, K. C.; Kim, T. S. Unveiling the Annealing-Dependent Mechanical Properties of Freestanding Indium Tin Oxide Thin Films. *ACS Appl Mater Interfaces* **2021**, *13* (14), 16650-16659. DOI: 10.1021/acsami.0c23112.

- (52) Zhou, J.; Zhang, X.; Zhang, X.; Zhang, W.; Li, J.; Chen, Y.; Liu, H.; Yan, Y. Mechanical Properties of Tensile Cracking in Indium Tin Oxide Films on Polycarbonate Substrates. *Coatings* **2022**, *12* (4). DOI: 10.3390/coatings12040538.
- (53) Hengst, C.; Menzel, S. B.; Rane, G. K.; Smirnov, V.; Wilken, K.; Leszczynska, B.; Fischer, D.; Prager, N. Mechanical Properties of ZTO, ITO, and a-Si:H Multilayer Films for Flexible Thin Film Solar Cells. *Materials (Basel)* **2017**, *10* (3). DOI: 10.3390/ma10030245.
- (54) Peng, C.; Jia, Z.; Bianculli, D.; Li, T.; Lou, J. In situ electro-mechanical experiments and mechanics modeling of tensile cracking in indium tin oxide thin films on polyimide substrates. *J Appl Phys* **2011**, *109* (10). DOI: 10.1063/1.3592341.
- (55) Kim, J.; Shrestha, S.; Souri, M.; Connell, J. G.; Park, S.; Seo, A. High-temperature optical properties of indium tin oxide thin-films. *Sci Rep* **2020**, *10* (1), 12486. DOI: 10.1038/s41598-020-69463-4.
- (56) Paine, D. C.; Whitson, T.; Janiac, D.; Beresford, R.; Yang, C. O.; Lewis, B. A study of low temperature crystallization of amorphous thin film indium–tin–oxide. *J Appl Phys* **1999**, *85* (12), 8445-8450. DOI: 10.1063/1.370695.
- (57) Guillén, C.; Herrero, J. Polycrystalline growth and recrystallization processes in sputtered ITO thin films. *Thin Solid Films* **2006**, *510* (1-2), 260-264. DOI: 10.1016/j.tsf.2005.12.273.
- (58) Guillén, C.; Herrero, J. Structure, optical, and electrical properties of indium tin oxide thin films prepared by sputtering at room temperature and annealed in air or nitrogen. *J Appl Phys* **2007**, *101* (7). DOI: 10.1063/1.2715539.
- (59) Pop, E. Energy Dissipation and Transport in Nanoscale Devices. *Nano Res* **2010**, *3* (3), 147-169. DOI: 10.1007/s12274-010-1019-z.
- (60) Hopkins, P. E. Thermal Transport across Solid Interfaces with Nanoscale Imperfections: Effects of Roughness, Disorder, Dislocations, and Bonding on Thermal Boundary Conductance. *ISRN Mechanical Engineering* **2013**, *2013*, 682586. DOI: 10.1155/2013/682586.
- (61) Cahill, D. G.; Braun, P. V.; Chen, G.; Clarke, D. R.; Fan, S.; Goodson, K. E.; Keblinski, P.; King, W. P.; Mahan, G. D.; Majumdar, A.; et al. Nanoscale thermal transport. II. 2003–2012. *Appl Phys Rev* **2014**, *1* (1). DOI: 10.1063/1.4832615.
- (62) Monachon, C.; Weber, L.; Dames, C. Thermal Boundary Conductance: A Materials Science Perspective. *Annu Rev Mater Res* **2016**, *46*, 433+. DOI: 10.1146/annurev-matsci-070115-031719.
- (63) Gaskins, J. T.; Hopkins, P. E.; Merrill, D. R.; Bauers, S. R.; Hadland, E.; Johnson, D. C.; Koh, D.; Yum, J. H.; Banerjee, S.; Nordell, B. J.; et al. Review—Investigation and Review of the Thermal, Mechanical, Electrical, Optical, and Structural Properties of Atomic Layer Deposited High-k Dielectrics: Beryllium Oxide, Aluminum Oxide, Hafnium Oxide, and Aluminum Nitride. *ECS Journal of Solid State Science and Technology* **2017**, *6* (10), N189-N208. DOI: 10.1149/2.0091710jss.
- (64) Gluch, J.; Röbler, T.; Menzel, S. B.; Eckert, J. Microstructure and stress in high-k Hf–Y–O thin films. *Microelectronic Engineering* **2011**, *88* (5), 561-563. DOI: 10.1016/j.mee.2010.06.043.
- (65) Pradhan, D. K.; Moore, D. C.; Francis, A. M.; Kupernik, J.; Kennedy, W. J.; Glavin, N. R.; Olsson, R. H.; Jariwala, D. Materials for high-temperature digital electronics. *Nature Reviews Materials* **2024**, *9* (11), 790-807. DOI: 10.1038/s41578-024-00731-9.

## SUPPORTING INFORMATION

# High-field Breakdown and Thermal Characterization of Indium Tin Oxide Transistors

Haotian Su<sup>1,†</sup>, Yuan-Mau Lee<sup>2,†</sup>, Tara Peña<sup>1</sup>, Sydney Fultz-Waters<sup>2</sup>, Jimin Kang<sup>1</sup>, Çağıl Köroğlu<sup>1</sup>, Sumaiya Wahid<sup>1</sup>, Christina J. Newcomb<sup>3</sup>, Young Suh Song<sup>1</sup>, H.-S. Philip Wong<sup>1</sup>, Shan X. Wang<sup>1,2</sup>, and Eric Pop<sup>1,2,4,5,\*</sup>

<sup>1</sup>Department of Electrical Engineering, Stanford University, Stanford, CA 94305, USA

<sup>2</sup>Department of Materials Science and Engineering, Stanford University, Stanford, CA 94305, USA

<sup>3</sup>Stanford Nano Shared Facilities, Stanford University, Stanford, CA 94305, USA

<sup>4</sup>Department of Applied Physics, Stanford University, Stanford, CA 94305, USA

<sup>5</sup>Precourt Institute for Energy, Stanford University, CA 94305, USA

<sup>†</sup>Authors contributed equally. \*Contact: [epop@stanford.edu](mailto:epop@stanford.edu)

### S1. Fabrication Process Flow

The fabrication process flow is illustrated in **Figure S1**. The process began with the dry thermal growth of a 100 nm SiO<sub>2</sub> layer on p<sup>++</sup> Si substrates. Subsequently, the 4 nm amorphous indium tin oxide (ITO) channel was deposited at room temperature using AJA magnetron sputtering, with a base pressure of  $2 \times 10^{-8}$  Torr or lower. ITO was RF-sputtered at 100 W in a 5 mTorr argon-oxygen (5:1) atmosphere, with a deposition rate of 9.6 Å/min. The ITO channel was then patterned by optical lithography (Heidelberg MLA150) and wet etching in a 1.7% HCl solution. A nickel (Ni) layer was deposited using a Kurt J. Lesker electron-beam evaporator at the Stanford Nano Shared Facilities (SNSF), with a base pressure of  $\sim 5 \times 10^{-8}$  Torr and a deposition rate of 1 Å/s. The deposition rates for all steps were calibrated using X-ray reflectivity. Finally, for scanning thermal microscopy (SThM) measurements, the devices were capped with a 6 nm Al<sub>2</sub>O<sub>3</sub> layer deposited via plasma-enhanced atomic layer deposition at 200 °C.

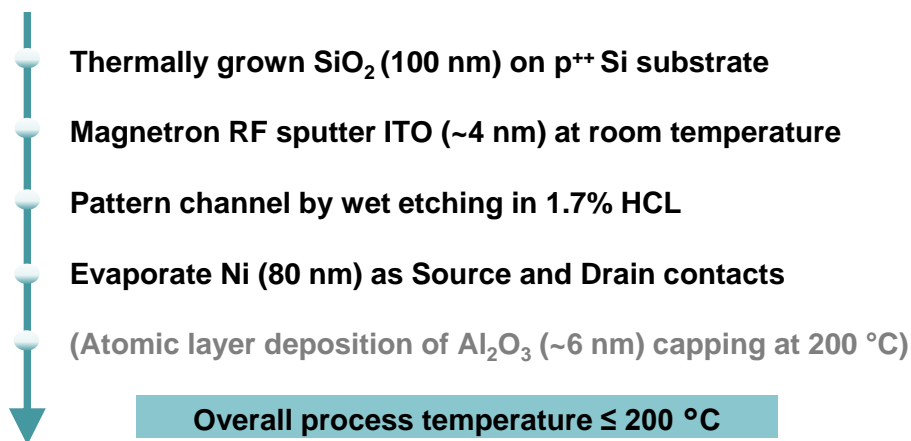


**Figure S1.** Fabrication process flow for ITO transistors, highlighting key steps. The entire process was conducted at temperatures  $\leq 200$  °C.



## S2. Additional Electrical Breakdown Characteristics

We conducted electrical breakdown measurements on ITO transistors under various biasing conditions; the transfer curves before and after breakdown are shown in **Figures S2a-e**. The transfer curves after breakdown under different breakdown biasing consistently exhibit a significant reduction in on-state  $I_D$  and loss of gate control. Gate leakage current ( $I_G$ ) was also monitored during all measurements and showed negligible change under breakdown conditions, as illustrated in **Figure S2f**. This suggests that the breakdown of ITO transistors is not due to gate dielectric breakdown.

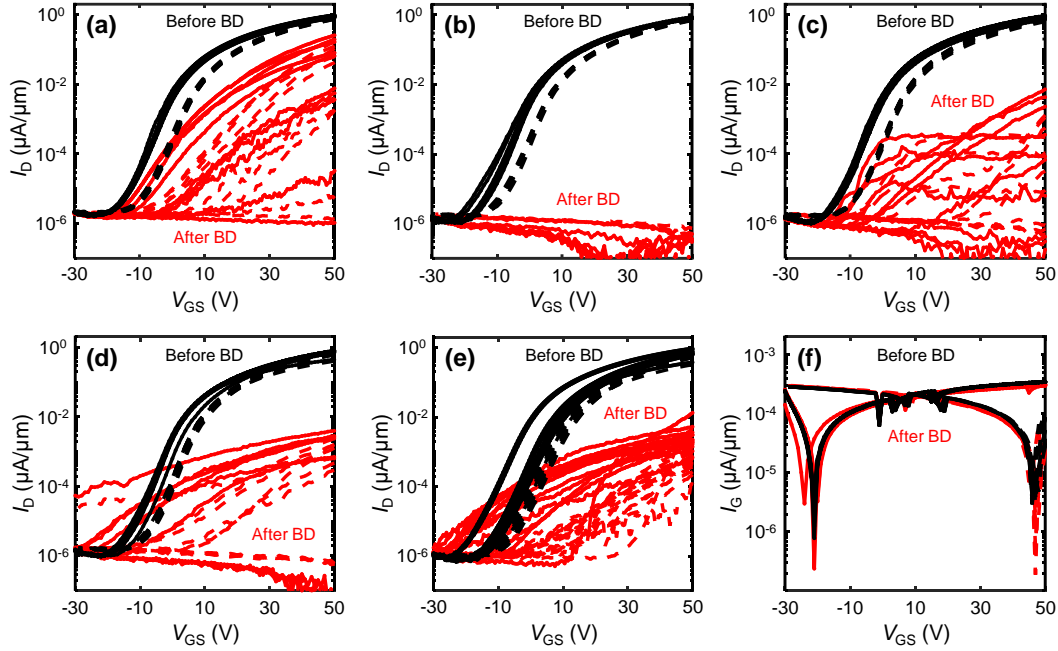


**Figure S2.** Transfer curves ( $I_D$  vs.  $V_{GS}$ , measured at  $V_{DS} = 0.1$  V) of ITO transistors measured before (black) and after breakdown (red) under different breakdown biasing conditions: **(a)**  $V_{GS} = -15$  V and  $V_{DS} = 40$  V; **(b)**  $V_{GS} = 0$  V and  $V_{DS} = 40$  V; **(c)**  $V_{GS} = 15$  V and  $V_{DS} = 40$  V; **(d)**  $V_{GS} = 60$  V and  $V_{DS} = 40$  V; **(e)**  $V_{GS} = 75$  V and  $V_{DS} = 25$  V. Each figure displays  $\sim 10$  measured devices. Transfer curves after breakdown demonstrate a significant reduction in on-state  $I_D$  and loss of gate control. All devices have channel length of  $1.6$   $\mu\text{m}$ . Solid/dashed lines are forward/backward  $V_{GS}$  sweeps. **(f)** Gate leakage current ( $I_G$ ) vs.  $V_{GS}$  before (black) and after (red) breakdown under  $V_{GS} = 45$  V and  $V_{DS} = 40$  V, showing similar trends for both cases, which rules out gate dielectric breakdown as the failure mechanism. (Note the different vertical axis scale, compared to the other figure panels.)

## S3. Scanning Thermal Microscopy (SThM) Details

We measured the temperature rise of ITO transistors using scanning thermal microscopy (SThM). The SThM setup consisted of a commercial module from Anasys® Instruments integrated with the MFP-3D AFM from Asylum Research. The SThM system employs a thermo-resistive probe connected to a Wheatstone bridge, a DC voltage source, and an amplifier specifically designed to minimize electrical spikes that could damage the probe.<sup>1-3</sup>

All measurements were performed in passive mode, where the sample was heated by electrical biasing, and the SThM tip recorded temperature-dependent changes in its electrical resistance. The SThM scans were conducted in contact mode at a setpoint of  $0.5$  V and a scan rate of  $0.8$  Hz. Measurements were performed at room temperature ( $\sim 20$  °C) in air under 20-30% humidity. This

technique allowed us to obtain nanoscale thermal maps of the sample surface. The thermal probe used in this work (PR-EX-GLA-5, from Anasys® Instruments) is made of a thin Pd layer on SiN.

The ITO transistors were capped with 6 nm Al<sub>2</sub>O<sub>3</sub> to prevent electrical shorting to the SThM probe. Although the SThM measures the surface temperature of this Al<sub>2</sub>O<sub>3</sub> rather than the underlying ITO channel, prior studies have shown that such thin capping layers have a negligible effect on the measurement,<sup>1,4</sup> because the surface temperature of the Al<sub>2</sub>O<sub>3</sub> layer closely matches the temperature of the ITO channel. To confirm this, we also conducted simulations with and without the capping layer, further verifying that the capping layer does not alter the temperature rise.

The SThM measurements produce a voltage signal ( $V_{\text{SThM}}$ ) that correlates with the sample surface temperature. To convert  $V_{\text{SThM}}$  to the corresponding temperature rise ( $\Delta T$ ), we previously calibrated the same SThM probes using samples with a set of Ti/Pd heaters of varying widths, as described by S. Deshmukh *et al.*<sup>3</sup> The conversion factor ( $F$ , with the unit of mV/K) is determined using the known temperature coefficient of resistance (TCR) of the metal lines. These heaters were capped with an Al<sub>2</sub>O<sub>3</sub> layer similar to that on our ITO transistors, to account for similar thermal (boundary) resistance at the probe-sample interface. While the conversion factor ( $F$ ) can vary between probes, these variations are more obvious only for measurements on sub-200 nm features.<sup>3</sup> For the micron-scale ITO transistors in this study,  $F$  remains consistent across probes. Based on our calibration, we adopted a conversion factor  $F = 7.0 \pm 0.5$  mV/K for this study.

#### S4. Finite-element Electro-Thermo-Mechanical Modeling

We estimate the temperature rise ( $\Delta T$ , above room temperature) of our ITO transistors using three-dimensional finite-element electro-thermo-mechanical modeling, through COMSOL Multiphysics®.<sup>5</sup> The steady-state simulations were conducted with the bottom of the Si substrate as the thermal ground (fixed at 293 K). To simplify the simulation, the ITO channel was modeled with a uniform sheet resistance across their width. Additionally, contact resistance is negligible in terms of heat generation because the ITO transistors in this study are sufficiently long<sup>6</sup> ( $L \approx 1.5$  to  $1.7$   $\mu\text{m}$ ). The thermal conductivity ( $k$ ) of the materials and thermal boundary conductance ( $G$ ) for various material interfaces used in our simulations are listed in **Table S1**. We also conducted the sensitivity analysis of  $\Delta T$  with respect to  $k$  and  $G$ , as shown in **Figures 5b-c** of the main text.

**Table S1.** Nominal thermal properties used in simulations, including thermal conductivity ( $k$ ) and thermal boundary conductance ( $G$ ) values, all near room temperature. Some specific  $G$  values not available in the literature were approximated by  $G$  values for pairs of similar and/or better-studied materials.<sup>5</sup>

Material	$k$ (Wm <sup>-1</sup> K <sup>-1</sup> )	Material Interface	$G$ (MWm <sup>-2</sup> K <sup>-1</sup> )
p <sup>+</sup> Si <sup>1,7</sup>	95	Si-SiO <sub>2</sub>	500
SiO <sub>2</sub> <sup>8,9</sup>	1.4	ITO-SiO <sub>2</sub>	50
ITO <sup>10-12</sup>	2	ITO-Ni	150
Ni <sup>13,14</sup>	40	Ni-Al <sub>2</sub> O <sub>3</sub>	150
Al <sub>2</sub> O <sub>3</sub> <sup>15,16</sup>	1.5	ITO-Al <sub>2</sub> O <sub>3</sub>	50
HfO <sub>2</sub> <sup>17-19</sup>	1.1	Si-HfO <sub>2</sub>	283
		ITO-HfO <sub>2</sub>	50

To investigate the strain distribution in ITO transistors during operation, we also conducted mechanical simulations by including the COMSOL thermal expansion module. The bottom of the Si

substrate was set as the fixed boundary and linear elastic material properties were assumed for all constituent materials. The nominal mechanical properties, including the coefficient of thermal expansion ( $\alpha$ ), Young's modulus ( $E$ ), and Poisson's ratio ( $\nu$ ), are listed in **Table S2**. Additionally, the initial stress induced by the Ni layer was accounted for in the simulations, with further details provided in Supporting Information **Section S5**.

**Table S2.** Nominal mechanical properties used in simulations, including the coefficient of thermal expansion ( $\alpha$ ), Young's modulus ( $E$ ), and Poisson's ratio ( $\nu$ ) for constituent materials in the ITO transistor.

Material	$\alpha$ (K <sup>-1</sup> )	$E$ (GPa)	$\nu$
SiO <sub>2</sub> <sup>20,21</sup>	$5.6 \times 10^{-7}$	70	0.17
HfO <sub>2</sub> <sup>22,23</sup>	$6 \times 10^{-6}$	250	0.25
ITO <sup>24-27</sup>	$8 \times 10^{-6}$	250	0.33
Ni <sup>28-31</sup>	$1.3 \times 10^{-5}$	200	0.30
Si <sup>20,21</sup>	$2.6 \times 10^{-6}$	170	0.28

### S5. Wafer-scale Ni Stress Characterization

An 80 nm Ni layer was deposited via electron-beam evaporation onto a 350  $\mu\text{m}$  thick (100) Si wafer with native oxide, under a base pressure of  $\sim 5 \times 10^{-8}$  Torr. The wafer curvature was measured both before and after metal deposition. Using the Stoney equation,<sup>32</sup> the stress in the Ni film was found to be  $\sim 75$  MPa. The thin film force was also determined, defined as  $F = \sigma t$ , where  $\sigma$  is the film stress and  $t$  is the film thickness. The measured Ni thin film force, summarized in **Table S3**, align well with the values reported in the literature.<sup>33,34</sup>

**Table S3.** Extracted stress and thin film force for the 80 nm Ni layer deposited as metal contacts.

Metal, nm	Stress (MPa)	Thin film force (N/m)
Ni, 80	75	6

### S6. Devices on 30 nm HfO<sub>2</sub> Dielectric

We also fabricated ITO transistors on 30 nm HfO<sub>2</sub> back-gate dielectric on Si (p<sup>++</sup>) back-gate substrates, as shown in **Figure S3a**, using the same fabrication flow detailed in Supporting Information **Section S1**. The 30 nm HfO<sub>2</sub> layer was deposited by plasma-enhanced atomic layer deposition at 200 °C, and its thickness was calibrated by ellipsometry. Measured electrical transfer curves and output characteristics are shown in **Figures S3b-c**. The Al<sub>2</sub>O<sub>3</sub> capping layer was found to induce a negative shift in the threshold voltage, consistent with our previous study.<sup>6</sup> Combining SThM and finite-element simulations, we determined the TBC between the ITO channel and the HfO<sub>2</sub> dielectric to be  $51 \pm 14 \text{ MWm}^{-2}\text{K}^{-1}$ , as shown in **Figure S3d**. **Figure S3e** shows the relationship between  $\Delta T_{\text{max}}$  and input power ( $P$ ), demonstrating good agreement between temperatures measured by SThM and simulated temperature at the breakdown power ( $P_{\text{BD}}$ ). The breakdown temperature ( $T_{\text{BD}}$ ) of ITO transistors on 30 nm HfO<sub>2</sub>/Si substrate is found to be  $\sim 272\text{-}340$  °C. This  $T_{\text{BD}}$  was nearly double that of devices on 100 nm SiO<sub>2</sub>/Si substrates. Mechanical simulations of strain distribution along the ITO channel **Figure S3f** revealed compressive strain under the contacts and tensile strain in the channel region under initial conditions. Under breakdown conditions, the peak compressive strain was observed near the channel edges. Our results show that ITO transistors on HfO<sub>2</sub> substrates exhibit significantly higher breakdown power, enabled by enhanced heat dissipation and closer thermal expansion matching between ITO and HfO<sub>2</sub>.

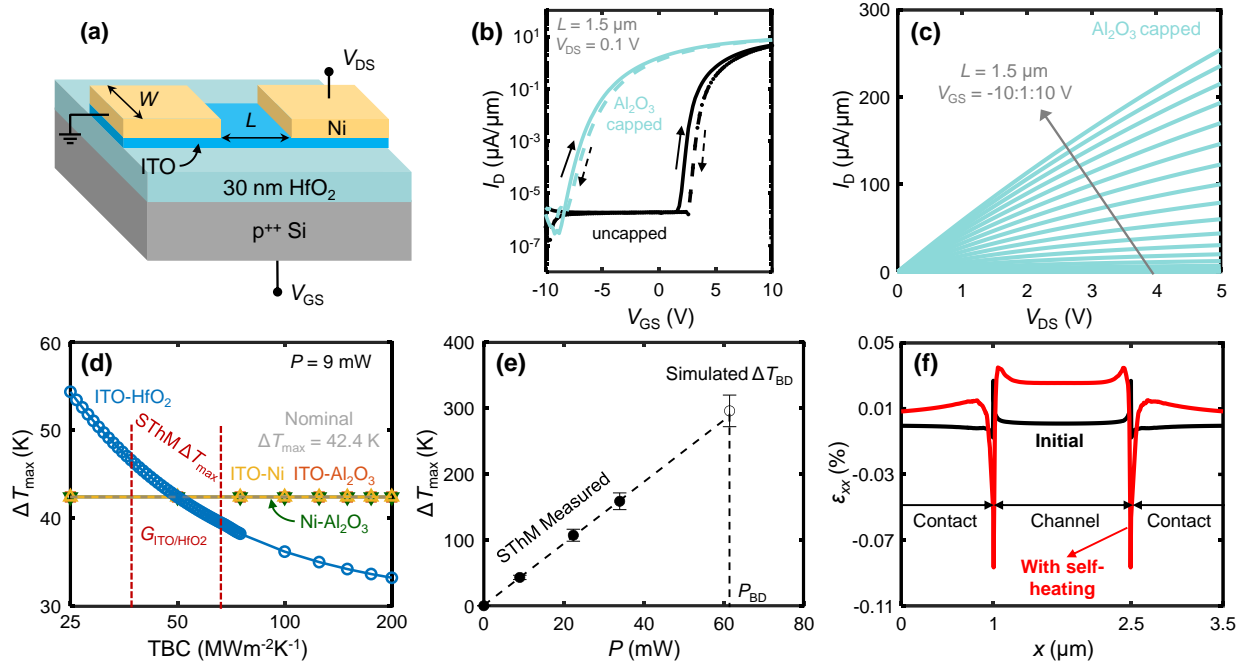


**Figure S3.** (a) Schematic of back-gated transistor, with 4 nm ITO channel on 30 nm HfO<sub>2</sub>/Si (p<sup>++</sup>) substrate, and 80 nm Ni source and drain contacts. (b) Measured transfer curves of uncapped (black) and Al<sub>2</sub>O<sub>3</sub>-capped (light blue) devices, showing negative shift in threshold voltage, similar to our previous work.<sup>6</sup> (c) Measured  $I_D$  vs.  $V_{DS}$  curve of Al<sub>2</sub>O<sub>3</sub>-capped devices, showing linear behavior. (d) Sensitivity analysis of  $\Delta T_{\max}$  with respect to TBC at material interfaces, showing minimal dependence on TBC at ITO-Ni, ITO-Al<sub>2</sub>O<sub>3</sub>, and Ni-Al<sub>2</sub>O<sub>3</sub> interfaces. However,  $\Delta T_{\max}$  varies with the TBC of the ITO-HfO<sub>2</sub> interface, estimated as  $51 \pm 14 \text{ MWm}^{-2}\text{K}^{-1}$  by comparing to the SThM measurements. (e) Dependence of  $\Delta T_{\max}$  on input power,  $P$ . Filled symbols mark SThM-measured temperature, hollow symbol is a simulation of  $\Delta T_{\max}$  at  $P_{BD}$ . Dashed line is a linear fit, to highlight the trend. (f) Initial strain distribution ( $\epsilon_{xx}$ ) along the channel direction, showing tensile strain in the ITO channel and compressive strain under contacts (black curve). At device breakdown with self-heating, the compressive strain peaks at the channel/contact edge (red curve).

## REFERENCES

- (1) Yalon, E.; McClellan, C. J.; Smithe, K. K. H.; Munoz Rojo, M.; Xu, R. L.; Suryavanshi, S. V.; Gabourie, A. J.; Neumann, C. M.; Xiong, F.; Farimani, A. B.; et al. Energy Dissipation in Monolayer MoS<sub>2</sub> Electronics. *Nano Lett* **2017**, *17* (6), 3429-3433. DOI: 10.1021/acs.nanolett.7b00252.
- (2) Datye, I. M.; Rojo, M. M.; Yalon, E.; Deshmukh, S.; Mleczko, M. J.; Pop, E. Localized Heating and Switching in MoTe<sub>2</sub>-Based Resistive Memory Devices. *Nano Lett* **2020**, *20* (2), 1461-1467. DOI: 10.1021/acs.nanolett.9b05272.
- (3) Deshmukh, S.; Rojo, M. M.; Yalon, E.; Vaziri, S.; Koroglu, C.; Islam, R.; Iglesias, R. A.; Saraswat, K.; Pop, E. Direct measurement of nanoscale filamentary hot spots in resistive memory devices. *Sci Adv* **2022**, *8* (13), eabk1514. DOI: 10.1126/sciadv.abk1514.
- (4) Swoboda, T.; Wainstein, N.; Deshmukh, S.; Koroglu, C.; Gao, X.; Lanza, M.; Hilgenkamp, H.; Pop, E.; Yalon, E.; Munoz Rojo, M. Nanoscale temperature sensing of electronic devices with calibrated scanning thermal microscopy. *Nanoscale* **2023**, *15* (15), 7139-7146. DOI: 10.1039/d3nr00343d.

- (5) Daus, A.; Vaziri, S.; Chen, V.; Köroğlu, Ç.; Grady, R. W.; Bailey, C. S.; Lee, H. R.; Schauble, K.; Brenner, K.; Pop, E. High-performance flexible nanoscale transistors based on transition metal dichalcogenides. *Nat Electron* **2021**, *4* (7), 495-501. DOI: 10.1038/s41928-021-00598-6.
- (6) Wahid, S.; Daus, A.; Kwon, J.; Qin, S.; Ko, J.-S.; Wong, H. S. P.; Pop, E. Effect of Top-Gate Dielectric Deposition on the Performance of Indium Tin Oxide Transistors. *IEEE Electron Device Letters* **2023**, *44* (6), 951-954. DOI: 10.1109/led.2023.3265316.
- (7) Asheghi, M.; Kurabayashi, K.; Kasnavi, R.; Goodson, K. E. Thermal conduction in doped single-crystal silicon films. *J Appl Phys* **2002**, *91* (8), 5079-5088. DOI: 10.1063/1.1458057.
- (8) Lee, S. M.; Cahill, D. G. Heat transport in thin dielectric films. *J Appl Phys* **1997**, *81* (6), 2590-2595. DOI: 10.1063/1.363923.
- (9) Zhu, W.; Zheng, G.; Cao, S.; He, H. Thermal conductivity of amorphous SiO<sub>2</sub> thin film: A molecular dynamics study. *Sci Rep* **2018**, *8* (1), 10537. DOI: 10.1038/s41598-018-28925-6.
- (10) Thuau, D.; Koymen, I.; Cheung, R. A microstructure for thermal conductivity measurement of conductive thin films. *Microelectronic Engineering* **2011**, *88* (8), 2408-2412. DOI: 10.1016/j.mee.2010.12.119.
- (11) Brinzari, V. I.; Cocemasov, A. I.; Nika, D. L.; Korotcenkov, G. S. Ultra-low thermal conductivity of nanogranular indium tin oxide films deposited by spray pyrolysis. *Appl Phys Lett* **2017**, *110* (7). DOI: 10.1063/1.4976629.
- (12) Cocemasov, A.; Brinzari, V.; Jeong, D. G.; Korotcenkov, G.; Vatavu, S.; Lee, J. S.; Nika, D. L. Thermal Transport Evolution Due to Nanostructural Transformations in Ga-Doped Indium-Tin-Oxide Thin Films. *Nanomaterials (Basel)* **2021**, *11* (5). DOI: 10.3390/nano11051126.
- (13) Zheng, X.; Cahill, D.; Krasnochtchekov, P.; Averbach, R.; Zhao, J. High-throughput thermal conductivity measurements of nickel solid solutions and the applicability of the Wiedemann–Franz law. *Acta Materialia* **2007**, *55* (15), 5177-5185. DOI: 10.1016/j.actamat.2007.05.037.
- (14) Cahill, D. G.; Braun, P. V.; Chen, G.; Clarke, D. R.; Fan, S.; Goodson, K. E.; Koblinski, P.; King, W. P.; Mahan, G. D.; Majumdar, A.; et al. Nanoscale thermal transport. II. 2003–2012. *Appl Phys Rev* **2014**, *1* (1). DOI: 10.1063/1.4832615.
- (15) Cappella, A.; Battaglia, J. L.; Schick, V.; Kusiak, A.; Lamperti, A.; Wiemer, C.; Hay, B. High Temperature Thermal Conductivity of Amorphous Al<sub>2</sub>O<sub>3</sub> Thin Films Grown by Low Temperature ALD. *Advanced Engineering Materials* **2013**, *15* (11), 1046-1050. DOI: 10.1002/adem.201300132.
- (16) Paterson, J.; Singhal, D.; Tainoff, D.; Richard, J.; Bourgeois, O. Thermal conductivity and thermal boundary resistance of amorphous Al<sub>2</sub>O<sub>3</sub> thin films on germanium and sapphire. *J Appl Phys* **2020**, *127* (24). DOI: 10.1063/5.0004576.
- (17) Panzer, M. A.; Shandalov, M.; Rowlette, J. A.; Oshima, Y.; Yi Wei, C.; McIntyre, P. C.; Goodson, K. E. Thermal Properties of Ultrathin Hafnium Oxide Gate Dielectric Films. *IEEE Electron Device Letters* **2009**, *30* (12), 1269-1271. DOI: 10.1109/led.2009.2032937.
- (18) Scott, E. A.; Gaskins, J. T.; King, S. W.; Hopkins, P. E. Thermal conductivity and thermal boundary resistance of atomic layer deposited high-k dielectric aluminum oxide, hafnium oxide, and titanium oxide thin films on silicon. *APL Materials* **2018**, *6* (5). DOI: 10.1063/1.5021044.
- (19) Scott, E. A.; Smith, S. W.; Henry, M. D.; Rost, C. M.; Giri, A.; Gaskins, J. T.; Fields, S. S.; Jaszewski, S. T.; Ihlefeld, J. F.; Hopkins, P. E. Thermal resistance and heat capacity in hafnium zirconium oxide (Hf<sub>1-x</sub>Zr<sub>x</sub>O<sub>2</sub>) dielectrics and ferroelectric thin films. *Appl Phys Lett* **2018**, *113* (19). DOI: 10.1063/1.5052244.
- (20) El-Kareh, B. *Fundamentals of Semiconductor Processing Technology*; 1995. DOI: 10.1007/978-1-4615-2209-6.

- (21) Jaikissoon, M.; Koroğlu, Ç.; Yang, J. A.; Neilson, K.; Saraswat, K. C.; Pop, E. CMOS-compatible strain engineering for monolayer semiconductor transistors. *Nat Electron* **2024**, *7* (10), 885-891. DOI: 10.1038/s41928-024-01244-7.
- (22) Gaskins, J. T.; Hopkins, P. E.; Merrill, D. R.; Bauers, S. R.; Hadland, E.; Johnson, D. C.; Koh, D.; Yum, J. H.; Banerjee, S.; Nordell, B. J.; et al. Review—Investigation and Review of the Thermal, Mechanical, Electrical, Optical, and Structural Properties of Atomic Layer Deposited High-k Dielectrics: Beryllium Oxide, Aluminum Oxide, Hafnium Oxide, and Aluminum Nitride. *ECS Journal of Solid State Science and Technology* **2017**, *6* (10), N189-N208. DOI: 10.1149/2.0091710jss.
- (23) Gluch, J.; Röbler, T.; Menzel, S. B.; Eckert, J. Microstructure and stress in high-k Hf–Y–O thin films. *Microelectronic Engineering* **2011**, *88* (5), 561-563. DOI: 10.1016/j.mee.2010.06.043.
- (24) Krataithong, C.; Srichai, K.; Wongrat, E.; Tubtimtae, A. Comparative study on the influence of transparent glass substrates for antimony telluride thin films via structural and optical properties. *Journal of Science: Advanced Materials and Devices* **2022**, *7* (3). DOI: 10.1016/j.jsamd.2022.100449.
- (25) Choi, S. K.; Lee, J. I. Effect of film density on electrical properties of indium tin oxide films deposited by dc magnetron reactive sputtering. *Journal of Vacuum Science & Technology A: Vacuum, Surfaces, and Films* **2001**, *19* (5), 2043-2047. DOI: 10.1116/1.1371326.
- (26) Hengst, C.; Menzel, S. B.; Rane, G. K.; Smirnov, V.; Wilken, K.; Leszczynska, B.; Fischer, D.; Prager, N. Mechanical Properties of ZTO, ITO, and a-Si:H Multilayer Films for Flexible Thin Film Solar Cells. *Materials (Basel)* **2017**, *10* (3). DOI: 10.3390/ma10030245.
- (27) Wittkowski, T.; Jorzick, J.; Seitz, H.; Schröder, B.; Jung, K.; Hillebrands, B. Elastic properties of indium tin oxide films. *Thin Solid Films* **2001**, *398-399*, 465-470. DOI: 10.1016/s0040-6090(01)01373-6.
- (28) Hoang, L.; Jaikissoon, M.; Koroglu, C.; Zhang, Z.; Bennett, R. K. A.; Song, J. H.; Yang, J. A.; Ko, J. S.; Brongersma, M. L.; Saraswat, K. C.; et al. Understanding the Impact of Contact-Induced Strain on the Electrical Performance of Monolayer WS<sub>2</sub> Transistors. *Nano Lett* **2024**, *24* (41), 12768-12774. DOI: 10.1021/acs.nanolett.4c02616.
- (29) Nix, F. C.; MacNair, D. The Thermal Expansion of Pure Metals: Copper, Gold, Aluminum, Nickel, and Iron. *Physical Review* **1941**, *60* (8), 597-605. DOI: 10.1103/PhysRev.60.597.
- (30) Pradhan, D. K.; Moore, D. C.; Francis, A. M.; Kupernik, J.; Kennedy, W. J.; Glavin, N. R.; Olsson, R. H.; Jariwala, D. Materials for high-temperature digital electronics. *Nature Reviews Materials* **2024**, *9* (11), 790-807. DOI: 10.1038/s41578-024-00731-9.
- (31) Ruud, J. A.; Josell, D.; Spaepen, F.; Greer, A. L. A New Method for Tensile Testing of Thin-Films. *Journal of Materials Research* **1993**, *8* (1), 112-117. DOI: Doi 10.1557/Jmr.1993.0112.
- (32) Janssen, G. C. A. M.; Abdalla, M. M.; van Keulen, F.; Pujada, B. R.; van Venrooy, B. Celebrating the 100th anniversary of the Stoney equation for film stress: Developments from polycrystalline steel strips to single crystal silicon wafers. *Thin Solid Films* **2009**, *517* (6), 1858-1867. DOI: 10.1016/j.tsf.2008.07.014.
- (33) Koch, R. Stress in Evaporated and Sputtered Thin Films – A Comparison. *Surface and Coatings Technology* **2010**, *204* (12-13), 1973-1982. DOI: 10.1016/j.surfcoat.2009.09.047.
- (34) Jaikissoon, M.; Pop, E.; Saraswat, K. C. Strain Induced by Evaporated-Metal Contacts on Monolayer MoS<sub>2</sub> Transistors. *IEEE Electron Device Letters* **2024**, *45* (8), 1528-1531. DOI: 10.1109/led.2024.3410095.